

Direct Simulations of Turbulent Flow Using Finite-Difference Schemes*

MAN MOHAN RAI

NASA Ames Research Center, Moffett Field, California

AND

PARVIZ MOIN

*Stanford University, Stanford, California and
NASA Ames Research Center, Moffett Field, California*

Received November 30, 1989; revised March 19, 1990

This paper presents finite-difference solutions to the evolution of small-amplitude disturbances and incompressible fully developed turbulent channel flow. The main objective of the paper is to provide a comprehensive comparison between the results obtained using finite-difference and spectral methods. An advantage of finite-difference schemes over the highly accurate spectral methods lies in the ease with which they can be applied to complex geometries. The finite-difference methods used include a kinetic-energy-conserving type of central difference scheme and a high-order-accurate upwind difference scheme. Unlike the central difference scheme, the upwind difference scheme was found not to require a kinetic energy conservation property to control aliasing error. The dissipative nature of the upwind scheme results in a damping of the higher frequency content. As a result very little energy is aliased back. The computed data (including first- and second-order statistics) for the turbulent channel flow case are found to compare well with experimental data and earlier spectral simulations. It appears that the high-order-accurate upwind scheme is a good candidate for direct simulations of turbulent flows over complex geometries. © 1991 Academic Press, Inc.

INTRODUCTION

Almost all of the current applied computational fluid dynamics (CFD) investigations using the Navier–Stokes equations require a model for computing turbulent stresses. In recent years CFD methods have been used to simulate the flow about extremely complicated configurations such as flow over a complete aircraft [1], unsteady flow through turbomachinery [2], flow through the SSME hot gas

* Originally presented as AIAA Paper No. 89-0369 at the AIAA 27th Aerospace Sciences Meeting held in Reno, Nevada, January 9–12, 1989.

manifold [3], and many other equally complicated flows. However, these computations rely on turbulence models that were developed using data obtained for simple flows. Even the more sophisticated turbulence models such as the $k-\varepsilon$ model [4], which are claimed to be more generally applicable than the simpler models such as the Baldwin-Lomax model [5], have not performed to expectations. The general experience among researchers has been that the performance of the $k-\varepsilon$ models has in many situations been no better than that obtained from the simpler models.

In many instances turbulence models have only a second-order effect on the computed solution, for example, surface pressures for certain simple supersonic external flows are computed with error values of less than 1% whereas heat transfer rates are computed with an error of about 15%. However, there are just as many situations where the turbulence model could have first-order effects on the solution, for example: (1) separated internal flows, where the calculated mass flow rate through the system is affected by the extent of the region of separation which is, in turn, dependent on the turbulence models; (2) transitional flows; and (3) flows at high angles of attack [6]. Whether one attempts to predict heat transfer rates more accurately or only reasonable surface pressure distributions, the major stumbling block is the predictive capability of the turbulence model.

In spite of the tremendous effort that has been put into developing turbulence models, progress in this area has been limited. The shortcoming of turbulence models used in most Reynolds-averaged Navier-Stokes computations is that they are designed to model all scales of turbulent structures. However, the larger scales are highly dependent on the particular geometry and flow conditions of interest; it is therefore difficult if not impossible to develop a universal turbulence model that accounts for all the scales of motion. A good compromise is to model only the smaller scales of motion. These scales, to a large extent, are the same in all flows and their structure is mainly determined by the energy they are required to dissipate. This technique is referred to as large eddy simulation (LES) because the larger eddies are calculated and the smaller ones are modeled (see, for example, Ref. [7]). In contrast, a *direct simulation* technique is one in which the grids used are sufficiently fine to resolve all scales of motion. The computing requirements for such an approach are excessively high for even moderate Reynolds numbers. However, direct simulations can be invaluable in guiding LES techniques (in the modeling of the smaller eddies) and in obtaining a fundamental understanding of the nature of turbulence [8].

To date the most successful direct simulations have been performed with spectral methods because of the very high accuracies of these methods [8]. However, spectral methods are difficult to use for complex geometries. They are also more complicated than finite-difference techniques and are not the prevailing methods in existing application codes. On the other hand, finite-difference methods are simple to implement and are also the most commonly used methods in current application codes. The major shortcoming of currently used finite-difference methods is that their accuracy levels are inadequate. The spectral element method attempts to retain the high accuracy of spectral methods and the geometric flexibility of finite-

difference and finite-element methods [9]. However, to the author's best knowledge this method has not yet been applied to turbulence simulations.

Earlier work in using finite-difference schemes in computing turbulent flow includes that of Deardorff [10], where fully developed, incompressible, turbulent channel flow at very large Reynolds numbers is calculated using an LES approach. Deardorff [10] uses the staggered grid approach of Harlow and Welch [11], the "leapfrog" method for time differencing, and central differences for the convective terms. A total of 6720 grid points, equally spaced in all directions, are used to compute the results that are presented. The computed results are found to be in rough agreement with the experimental results of Laufer [12]. The differences between theory and experiment can be attributed to the extremely coarse grid used, the differences in Reynolds number, and deficiencies in the modeling of the subgrid scale (SGS) Reynolds stresses. Schumann [13] presents results for incompressible fluid flow in plane channels and concentric annuli using a LES approach and a finite-difference integration scheme. The finite-difference scheme for the gross scale velocities is essentially the same as that used in Ref. [10]. Both of these schemes are momentum- and energy-conserving. The results of Ref. [13] are obtained using a different SGS model, higher grid resolution, and larger values of the channel streamwise and spanwise lengths (as compared to Ref. [10]). The computed mean velocity profile and some first-order turbulence statistics are found to be in good agreement with the experimental data of Refs. [12, 14]. Schumann [13] makes the important observation that while the finite-difference scheme is energy conserving, the actual energy transfer toward larger wave numbers in the simulation of the gross scales is too large.

Herring *et al.* [15] present computed results for the decay of two-dimensional, homogeneous, isotropic, incompressible turbulence. The calculations are performed using a vorticity and stream function approach and both spectral and finite-difference integration methods. Although this technique is quite different from the one that is used in the present study (the governing equations are written using the primitive variables), two important conclusions given in Ref. [15] do pertain to the current situation: (1) spectral methods signal their accuracy or inaccuracy through an inadequately resolved enstrophy dissipation spectrum whereas finite-difference schemes do not; and (2) spectral methods require roughly half as much resolution as finite-difference schemes in each spatial direction (the finite-difference scheme used in Ref. [15] is second-order accurate) to yield solutions of comparable accuracy.

In the past, efforts towards developing higher-order accurate finite-difference methods were frustrated because of the lack of robustness of the new schemes. Even the lower order methods required a few arbitrary smoothing parameters or an energy conservation principle (which is difficult to realize on general grids) to stabilize them. However, modern upwind schemes are found to be extremely robust even when they are made high-order accurate (Ref. [16]). For this reason they hold some promise of being able to simulate turbulent flows over complex geometries with general boundary conditions. The purpose of this study is to evaluate the

performance of such high-order-accurate upwind methods and other finite-difference schemes in simulating turbulent flow and accurately predicting the higher-order statistics of such flows.

In the following section, a spatially high-order-accurate, upwind-biased finite-difference scheme is developed for the incompressible Navier–Stokes equations in three dimensions. The scheme uses a staggered grid as in Ref. [11] and is a variant of the partially implicit, fractional-step approach of Ref. [17]. The accuracy of the integration method is first tested by computing the evolution of small-amplitude disturbances in channel flow. The scheme is then used to compute fully developed channel flow at a Reynolds number of 180 (based on wall shear velocity and channel half-width). The results of these investigations are compared with experimental data and the spectral calculations of Ref. [8]. The implicit smoothing of the upwind-biased scheme is found to control aliasing errors without unduly affecting the accuracy of the solution for reasonable grid sizes.

Results are also presented for a second-order-accurate central difference scheme of the type developed in Ref. [11]. The inadequacy of the second-order accuracy of the scheme (for the grid size chosen) is demonstrated using the test cases mentioned above. An additional limitation of this scheme is that in order to be stable it must be kinetic-energy conserving in nature. Deviations in the differencing technique that retained second-order accuracy but not the energy conservation principle resulted in unstable solutions.

THE NUMERICAL METHOD

The integration method used in this study is based on a partially implicit, fractional step method developed in Ref. [17]. The method of Ref. [17] is a variant of the fractional step method of Ref. [18]. In this section, the method of Ref. [17] is briefly outlined and then the high-order accurate upwind-biased method is presented.

The conservative form of the continuity and momentum equations for incompressible flow are given by

$$\frac{\partial u_i}{\partial x_i} = 0 \quad (1)$$

and

$$\frac{\partial u_i}{\partial t} + \frac{\partial}{\partial x_j} u_i u_j = -\frac{\partial p}{\partial x_i} + \frac{1}{\text{Re}} \frac{\partial}{\partial x_j} \frac{\partial}{\partial x_j} u_i \quad (2)$$

where u_1, u_2, u_3 are velocities in the x_1, x_2, x_3 directions, respectively, p is the pressure, and Re is the Reynolds number. The dependent variables in Eqs. (1) and

(2) have been nondimensionalized by a characteristic velocity and length scale. The fractional step method of Ref. [17] is given by

$$\frac{\hat{u}_i - u_i^n}{\Delta t} = \frac{1}{2} (3H_i^n - H_i^{n-1}) + \frac{1}{2\text{Re}} \left(\frac{\delta^2}{\delta x_1^2} + \frac{\delta^2}{\delta x_2^2} + \frac{\delta^2}{\delta x_3^2} \right) (\hat{u}_i + u_i^n) \quad (3)$$

$$\frac{u_i^{n+1} - \hat{u}_i}{\Delta t} = -G(\phi^{n+1}) \quad (4)$$

with

$$D(u_i^{n+1}) = 0, \quad (5)$$

where H_i represents the convective terms, G and D represent discrete gradient and divergence operators, respectively, and $\delta^2/\delta x_j^2$ represent finite-difference operators for the second derivatives. The variable ϕ is related to the pressure and is given by

$$\phi - \frac{\Delta t}{2\text{Re}} \nabla^2 \phi = p. \quad (6)$$

The solution procedure consists of the following steps: (1) calculate intermediate velocities \hat{u}_i using Eq. (3); (2) calculate the pressure related variable ϕ by solving Eq. (4) (the unknown velocities u_i^{n+1} in Eq. (4) can be eliminated by taking the divergence of both sides of this equation and using Eq. (5)); and (3) calculate the velocities at the new time level (u_i^{n+1}) using Eq. (4). The scheme outlined in Eqs. (3)–(5) uses a second-order accurate explicit, Adams–Bashforth scheme for the convective terms and the second-order accurate, implicit, Crank–Nicolson scheme for the viscous terms. An approximate factorization technique is used to solve Eq. (3). The spatial derivatives in Eqs. (3)–(5) are evaluated using central differences on a staggered grid. As observed in Ref. [17], the use of staggered grids eliminates the need for ad hoc pressure boundary conditions. The method used in this study differs from that of Ref. [17] in several ways. The modifications to the scheme of Ref. [17] have been made to meet specific goals and are outlined below.

Aliasing Error and Upwind Differences

One of the problems encountered in direct simulations of turbulent flow is the control of aliasing error. Use of schemes which do not have a mechanism of controlling aliasing error can result in the decay of the turbulence in a given flow field or an unbounded growth of the solution. One approach to overcoming this problem is to use energy conserving schemes. The method of Ref. [17], approximating the convective derivatives as in Ref. [11], conserves the total kinetic energy in the grid (in the absence of the viscous terms) and therefore can be used for direct simulations of turbulence. However, while energy is conserved by this

scheme, it is not clear how this energy is redistributed. A second method of controlling aliasing error is to extract and discard at each time step that energy which would otherwise be aliased back. However, current procedures that perform this operation rely on series representations of the dependent variables (such as Fourier representations), and it is not clear how these procedures can be extended to curvilinear grids. A more detailed discussion of the role of aliasing error in fluid dynamical calculations and techniques for the removal of aliasing error can be found in Ref. [19].

For the reasons outlined above, the present method uses an upwind differencing technique for the convective terms in Eq. (3). The leading truncation error term of some upwind differences is dissipative in nature and thus damps the higher frequency content. Since only the energy in the upper portion of the spectrum is aliased back, a dissipation of the energy content of this part of the spectrum (due to the natural smoothing of the upwind scheme) results in significant control of aliasing errors. The main disadvantage is that the useful information in the upper portion of the spectrum is also lost in the process. However, this problem can be overcome with the use of additional grid points. The upwind technique (like other finite-difference techniques) also has the advantage that it can be used for curvilinear grids. For this reason the convective terms in Eq. (3) are evaluated using upwind differences (as before, the viscous terms are approximated using central differences).

First-order accurate upwind differences are extremely dissipative in nature and are hence of little use in practical applications. Second-order accurate upwind methods are considerably less dissipative and are widely used in application codes. However, even second-order accuracy can be insufficient for direct simulations of turbulence (this will be demonstrated in a later section). In this study we use a fifth-order accurate difference scheme for the convective terms. However, first one particular aspect of upwind differences will be considered, that is, the size of the stencil (the number of consecutive grid points) required to achieve a certain order of accuracy. It can be shown that $2n + 1$ grid points are required to produce n th-order accurate upwind differences (this estimate takes into account that both forward and backward differences of a given quantity may be required at any grid point). This requirement translates into a 11-point stencil in order to produce fifth-order accurate upwind differences. The problem with such large stencils is that many grid points near the computational boundaries can no longer be treated using the finite differences used in the interior; therefore they will require special treatment. Hence, finite differences are needed that are as compact as possible subject to the constraint that they have the desirable natural smoothing that controls aliasing errors.

Upwind-biased differences require a much smaller stencil than fully upwind differences to obtain a given order of accuracy. In addition, the upwind-biased differences used in this study have the desired natural dissipation to control aliasing error. Upwind-biased differences achieve a higher order of accuracy for a given stencil size by using grid points on either side of the point in question but with more points in the direction in which the difference is to be biased. For example, a decision to use at most five grid points (two on either side of the point at which

the derivative is to be calculated) would result in a second-order accurate fully upwind (backward) difference for a first derivative

$$\left(\frac{\partial u}{\partial x}\right)_j = \frac{3u_j - 4u_{j-1} + u_{j-2}}{2\Delta x},$$

whereas the same derivative could be computed to third-order accuracy using upwind-biased differences as follows:

$$\left(\frac{\partial u}{\partial x}\right)_j = \frac{2u_{j+1} + 3u_j - 6u_{j-1} + u_{j-2}}{6\Delta x}.$$

The extra accuracy is obtained because of the additional data point used in the approximation. The use of the entire stencil would result in a fourth-order-accurate central difference without natural dissipation. The high-order accurate method of this study uses a seven-point stencil and fifth-order accurate upwind-biased differences.

Time-Stepping Procedure

As mentioned earlier, the method of Ref. [17] uses a second-order accurate, explicit, Adams–Bashforth method for the convective terms. A simple Fourier stability analysis of this method as applied to the one-dimensional linear convection equation

$$\frac{\partial u}{\partial t} + c \frac{\partial u}{\partial x} = 0 \quad (7)$$

shows that it is unstable for all CFL numbers. However, the instability is very weak and the method usually works for CFL numbers less than 1.0 in the presence of a viscous term on the right-hand side of Eq. (7). The Runge–Kutta methods seem more suitable for the convective terms because of their stability. The low-storage Runge–Kutta methods of Ref. [20] have the additional advantage that they require the minimum amount of computer run-time memory for this class of schemes. In this study we use a three-step hybrid Runge–Kutta/Crank–Nicholson scheme developed by Spalart (private communication) that is a variant of the three-step, low-storage, Runge–Kutta method developed in Ref. [20]. The method of Spalart uses an explicit Runge–Kutta method for the convective terms and an implicit Crank–Nicholson method for the viscous terms of Eq. (3). The method is second-order accurate in time for the viscous terms and third-order accurate in time for the convective terms, the overall accuracy being second order in time.

Spatial Order of Accuracy

Another important issue is the spatial order of accuracy of finite-difference methods on nonuniform grids. The accuracy of most finite-difference methods is

defined for equispaced grids. These finite-difference methods are then used on stretched meshes or even curvilinear meshes under the assumption that the accuracy of the method does not suffer appreciably in the process. In reality, the accuracy could drop. A simple example would be the approximation of the term $\partial u / \partial x$ using central differences and a three-point stencil. On an equispaced mesh this could be performed as follows:

$$\frac{\partial u}{\partial x} = \frac{u_{j+1} - u_{j-1}}{2\Delta x} + O(\Delta x)^2. \quad (8)$$

The above approximation is second-order accurate. A commonly used extension of this technique on a stretched mesh involves defining the transformation

$$\xi = \xi(x) \quad (9)$$

and determining $\partial u / \partial x$ from

$$\frac{\partial u}{\partial x} = \frac{\partial u}{\partial \xi} \frac{\partial \xi}{\partial x}, \quad (10)$$

where the terms $\partial u / \partial \xi$ and $\partial \xi / \partial x$ are approximated as

$$\begin{aligned} \frac{\partial u}{\partial \xi} &= \frac{u_{j+1} - u_{j-1}}{2\Delta \xi} \\ \frac{\partial \xi}{\partial x} &= \frac{2\Delta \xi}{x_{j+1} - x_{j-1}}. \end{aligned} \quad (11)$$

This approach leads to a second-order accurate approximation to $\partial u / \partial x$ only if the transformation defined in Eq. (9) is sufficiently smooth (in this case, a continuous second derivative). For grids where the spacing does not vary smoothly, second-order accuracy can be obtained only from an approximation that takes into account the stretching of the mesh, that is,

$$\frac{\partial u}{\partial x} = \frac{u_{j+1} + (a^2 - 1)u_j - a^2 u_{j-1}}{a(a+1)(x_j - x_{j-1})}, \quad (12)$$

where

$$a = (x_{j+1} - x_j) / (x_j - x_{j-1}).$$

Since the ultimate objective of the current effort is to develop a methodology that can be used for direct simulations of turbulent flow over general geometries (where generating grids that are sufficiently smooth is difficult), and, since accurate direct simulations of turbulence requires high-order accuracy (this will be demonstrated in the results section of this paper), difference formulas of the type given in Eq. (12)

are used in this study. The convective and viscous terms in the momentum equations, the divergence operator in the continuity equation, and the gradient of the pressure in the momentum equation are all obtained by using high-order accurate finite-differences that take into account the stretching of the mesh.

A Note on the Conservation of Fluxes in a Discrete Sense

Reference [17] uses the conservative form of the governing equations and a finite-difference scheme that conserves mass and momentum in a discrete sense. To illustrate the conservation property we consider the inviscid Burgers equation in one spatial dimension:

$$\begin{aligned}\frac{\partial u}{\partial t} + \frac{\partial f}{\partial x} &= 0 \\ f &= f(u) = \frac{u^2}{2}\end{aligned}\tag{13}$$

and a fully implicit finite-difference approximation to it

$$\frac{u_j^{n+1} - u_j^n}{\Delta t} + \frac{\hat{f}_{j+1/2}^{n+1} - \hat{f}_{j-1/2}^{n+1}}{\Delta x} = 0,\tag{14}$$

where the $\hat{f}_{j+1/2}$ terms represent numerical fluxes consistent with the physical flux f , and, for a central difference scheme are given by

$$\hat{f}_{j+1/2}^{n+1} = 0.5 \left(\frac{u_j^{n+1} + u_{j+1}^{n+1}}{2} \right)^2.\tag{15}$$

The scheme as given by Eqs. (14) and (15) is second-order accurate in space on an equispaced grid and satisfies the global conservation property because the numerical fluxes telescope; that is, given a set of consecutive grid points $r \cdots s$, the sum

$$S = \sum_{k=r}^{k=s} \frac{\Delta x}{\Delta t} (u_k^{n+1} - u_k^n) = - \sum_{k=r}^{k=s} (\hat{f}_{k+1/2}^{n+1} - \hat{f}_{k-1/2}^{n+1})\tag{16}$$

reduces to

$$S = \hat{f}_{r-1/2}^{n+1} - \hat{f}_{s+1/2}^{n+1}.\tag{17}$$

Clearly, a direct extension of this approach to a stretched mesh with the numerical fluxes defined as in Eq. (15) but with the finite-difference scheme redefined as

$$\frac{u_j^{n+1} - u_j^n}{\Delta t} + \frac{\hat{f}_{j+1/2}^{n+1} - \hat{f}_{j-1/2}^{n+1}}{0.5(x_{j+1} - x_j) + 0.5(x_j - x_{j-1})} = 0\tag{18}$$

yields a globally conservative scheme that is second-order accurate on stretched grids when the stretching is sufficiently smooth. Modification of this scheme to make it higher-order accurate on generalized grids without losing the global conservation property is not straightforward. In this study we defer this issue and use the nonconservative form of the equations for which high order accuracy can be achieved in a relatively straightforward manner. Since the flows under consideration do not contain shocks and other flow discontinuities, the nonconservative form of the equations should perform as well as the conservative form of the equations. However, the issue of obtaining high order accuracy subject to the constraint of conserving fluxes globally is one that will have to be addressed before direct or large eddy simulations of flows that contain discontinuities can be performed.

The Current Method

Having discussed the modifications made to the fractional step scheme of Ref. [17] in obtaining the scheme used in the present study and the reasons for these modifications, we now describe the high-order accurate, partially implicit, upwind-biased, fractional step scheme. The nonconservative form of the continuity and momentum equations for incompressible flow are given by

$$\frac{\partial u_i}{\partial x_i} = 0 \quad (19)$$

and

$$\frac{\partial u_i}{\partial t} + u_j \frac{\partial}{\partial x_j} u_i = -\frac{\partial p}{\partial x_i} + \frac{1}{\text{Re}} \frac{\partial}{\partial x_j} \frac{\partial}{\partial x_j} u_i. \quad (20)$$

The three-step Runge–Kutta scheme to solve Eqs. (19) and (20) is given by

Step 1.

$$\begin{aligned} u_i^a &= u_i^n + \Delta t \left(\gamma_1 H_i(u_i^n) + \frac{\alpha_1}{\text{Re}} \left(\frac{\delta^2}{\delta x_1^2} + \frac{\delta^2}{\delta x_2^2} + \frac{\delta^2}{\delta x_3^2} \right) (u_i^n + u_i^n) \right) \\ \frac{\tilde{u}_i - u_i^a}{\Delta t} &= -G(\gamma_1 \phi) \\ D(\tilde{u}_i) &= 0, \end{aligned} \quad (21a)$$

Step 2.

$$\begin{aligned} u_i^b &= \tilde{u}_i + \Delta t \left(\gamma_2 H_i(\tilde{u}_i) + \zeta_1 H_i(u_i^n) + \frac{\alpha_2}{\text{Re}} \left(\frac{\delta^2}{\delta x_1^2} + \frac{\delta^2}{\delta x_2^2} + \frac{\delta^2}{\delta x_3^2} \right) (\tilde{u}_i + u_i^b) \right) \\ \frac{\tilde{\tilde{u}}_i - u_i^b}{\Delta t} &= -G(\gamma_2 \tilde{\phi} + \zeta_1 \phi) \\ D(\tilde{\tilde{u}}_i) &= 0, \end{aligned} \quad (21b)$$

Step 3.

$$\begin{aligned}
 u_i^c &= \tilde{u}_i + \Delta t \left(\gamma_3 H_i(\tilde{u}_i) + \zeta_2 H_i(\tilde{u}_i) + \frac{\alpha_3}{\text{Re}} \left(\frac{\delta^2}{\delta x_1^2} + \frac{\delta^2}{\delta x_2^2} + \frac{\delta^2}{\delta x_3^2} \right) (\tilde{u}_i + u_i^c) \right) \\
 \frac{u_i^{n+1} - u_i^c}{\Delta t} &= -G(\gamma_3 \tilde{\phi} + \zeta_2 \tilde{\phi}) \\
 D(u_i^{n+1}) &= 0,
 \end{aligned} \tag{21c}$$

where

$$\begin{aligned}
 \alpha_1 &= 4/15 \\
 \alpha_2 &= 1/15 \\
 \alpha_3 &= 1/6 \\
 \gamma_1 &= 8/15 \\
 \gamma_2 &= 5/12 \\
 \gamma_3 &= 3/4 \\
 \zeta_1 &= -17/60 \\
 \zeta_2 &= -5/12.
 \end{aligned} \tag{22}$$

G and D are discrete gradient and divergence operators as before, and H_i represents the nonconservative form of the convective terms. Each of three steps outlined above closely resembles the fractional step method described in Eqs. (3)–(5). The predictor step in Eqs. (21a), (21b), and (21c) is solved using an approximate factorization method. For the channel flow calculations presented later in this study, the mean pressure gradient was added to the predictor step of Eqs. (21a), (21b), and (21c). The Poisson equation resulting from the corrector steps (in conjunction with the divergence-free property) is solved using transform methods. This approach is discussed in detail in Ref. [17] and therefore will not be discussed here.

The convective terms H_i are approximated using high-order accurate upwind-biased differences; for example, the first term in the u_1 momentum equation is evaluated as

$$\begin{aligned}
 u_1(u_1)_{x_1} &= (u_1)_i (-6(u_1)_{i+2} + 60(u_1)_{i+1} + 40(u_1)_i \\
 &\quad - 120(u_1)_{i-1} + 30(u_1)_{i-2} - 4(u_1)_{i-3}) / (120\Delta x_1)
 \end{aligned}$$

if $u_1 > 0$ and

$$\begin{aligned}
 u_1(u_1)_{x_1} &= (u_1)_i (4(u_1)_{i+3} - 30(u_1)_{i+2} + 120(u_1)_{i+1} \\
 &\quad - 40(u_1)_i - 60(u_1)_{i-1} + 6(u_1)_{i-2}) / (120\Delta x_1)
 \end{aligned} \tag{23}$$

if $u_1 < 0$, on a grid that is equispaced in the x_1 direction. The remaining convective terms are evaluated in a similar manner. The viscous terms are evaluated using central differences. For stretched meshes (the type used in the wall-to-wall direction for channel flow), the coefficients in the difference formulae are evaluated numerically in the code using Lagrange polynomials so as to retain high-order accuracy even on grids where the underlying transformation is not sufficiently smooth (obtaining explicit formulas for these coefficients becomes a laborious task for anything more than second-order accurate differences). In general, different stencil sizes will have to be used to obtain the same order of accuracy for the first and second derivatives (convective and viscous terms) in the integration method. In the present study a maximum of seven consecutive grid points (three on either side of the point in question) are used in the evaluation of the convective and viscous derivatives. With a seven-point stencil, the convective and viscous terms are approximated to fifth- and sixth-order accuracy, respectively.

Figure 1 shows the two-dimensional counterpart of the three-dimensional staggered grid that was used to obtain the results of this study. The velocities u_1 and u_2 are defined at the midpoints of the vertical and horizontal sides of each cell, respectively, and the pressure is defined at the midpoint of each cell. The second-order accurate divergence operator of Ref. [17] is defined at the midpoints of the cells and is given by

$$D_{i,j} = \frac{(u_1)_{i+1/2,j} - (u_1)_{i-1/2,j}}{\Delta x_1} + \frac{(u_2)_{i,j+1/2} - (u_2)_{i,j-1/2}}{\Delta x_2}. \quad (24)$$

The second-order accurate gradient operator of Ref. [17] is defined at the midpoints of the cell sides and is given by

$$\begin{aligned} (\phi_{x_1})_{i+1/2,j} &= \frac{\phi_{i+1,j} - \phi_{i,j}}{\Delta x_1} \\ (\phi_{x_2})_{i,j+1/2} &= \frac{\phi_{i,j+1} - \phi_{i,j}}{\Delta x_2}. \end{aligned} \quad (25)$$

This combination of the divergence and gradient operators results in a three-point stencil in each spatial direction for the Laplacian of ϕ which arises during the process of obtaining ϕ . In the present method, the divergence operator is once again defined at the cell centers but the spatial derivatives of this operator are defined using a stencil size of four. Thus, on an equispaced grid, this operator takes the form

$$\begin{aligned} D_{i,j} &= [- (u_1)_{i+3/2,j} + 27(u_1)_{i+1/2,j} \\ &\quad - 27(u_1)_{i-1/2,j} + (u_1)_{i-3/2,j}]/(24\Delta x_1) \\ &\quad + [- (u_2)_{i,j+3/2} + 27(u_2)_{i,j+1/2} \\ &\quad - 27(u_2)_{i,j-1/2} + (u_2)_{i,j-3/2}]/(24\Delta x_2). \end{aligned} \quad (26)$$

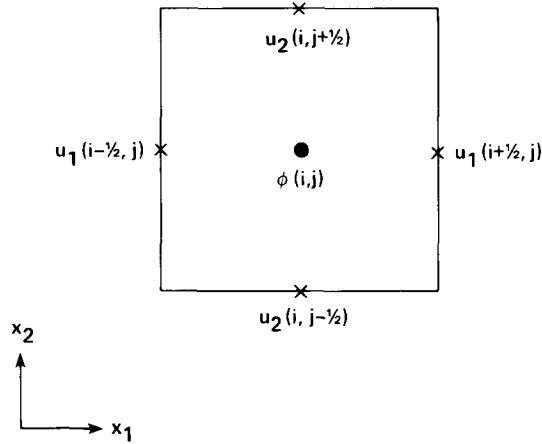


FIG. 1. Staggered grid showing physical locations at which the dependent variables are defined.

The Lagrange polynomial method is used to obtain the coefficients of the divergence operator for stretched meshes. The gradient operator is defined in a similar manner using four grid points in each direction. Consequently, the Laplacian of ϕ is defined on a stencil of seven grid points in each spatial direction (consistent with the self-imposed constraint mentioned earlier). With the four-point stencils mentioned above, it can be shown that the divergence and gradient operators are approximated to fourth-order accuracy on sufficiently smooth grids and to third-order accuracy otherwise.

As shown in Fig. 1, the components of the velocity are defined at different physical locations. Consequently the u_1 , u_2 , and u_3 momentum equations are integrated at the $(i + \frac{1}{2}, j, k)$, $(i, j + \frac{1}{2}, k)$, and $(i, j, k + \frac{1}{2})$ locations, respectively. Considering the u_1 momentum equation, we see that the convective terms of this equation require the u_2 and u_3 velocity components to be defined at the $(i + \frac{1}{2}, j, k)$ locations. A linear interpolation procedure (second-order accurate) is used in Ref. [17] to obtain these velocity components. The method used in this study uses a cubic interpolation technique (fourth-order accurate).

Whereas the integration scheme is high-order accurate at the interior grid points, the overall accuracy of the scheme is reduced because of the manner in which the boundary conditions are implemented and the unavailability of large stencils near boundaries. The conventional ways of treating boundary and near-boundary grid points are usually consistent with the second-order accuracy of many of the schemes in current use. When these conventional ways are used with the high-order scheme developed in this study, the overall accuracy of the scheme is reduced. However, results thus obtained appear far superior to those obtained with conventional second-order schemes (in spite of the drop in overall accuracy). No attempt has been made in this study to improve the accuracy of the boundary conditions

used. Grid points that are next to the boundary are treated using either three-point central differences or a third-order accurate upwind-biased scheme, depending on the size of the stencil available.

To describe the wall boundary procedure in greater detail we consider the point $(i, j - \frac{1}{2})$ in Fig. 1 as a point on a wall boundary. In order to simplify the description of the boundary procedure we assume an equispaced grid. The divergence operator for the cell (i, j) is taken to be

$$\begin{aligned} D_{i,j} = & [- (u_1)_{i+3/2,j} + 27(u_1)_{i+1/2,j} \\ & - 27(u_1)_{i-1/2,j} + (u_1)_{i-3/2,j}] / (24\Delta x_1) \\ & + [(u_2)_{i,j+1/2} - (u_2)_{i,j-1/2}] / (\Delta x_2) \end{aligned} \quad (27)$$

which is fourth-order accurate in x_1 and second-order accurate in x_2 . The x_1 component of the gradient operator is computed using the fourth-order accurate finite difference given as

$$(\phi_{x_1})_{i+1/2,j} = \frac{-\phi_{i+2,j} + 27\phi_{i+1,j} - 27\phi_{i,j} + \phi_{i-1,j}}{24\Delta x_1} \quad (28)$$

and the x_2 component of the gradient operator is computed using the following second-order accurate finite-difference

$$(\phi_{x_2})_{i,j+1/2} = \frac{\phi_{i,j+1} - \phi_{i,j}}{\Delta x_2}. \quad (29)$$

The corrector step of Eq. (21a) for the points $(i - \frac{3}{2}, j)$, $(i - \frac{1}{2}, j)$, $(i + \frac{1}{2}, j)$, $(i + \frac{3}{2}, j)$, and $(i, j + \frac{1}{2})$ can be written as

$$\begin{aligned} \frac{(\tilde{u}_1)_{i-3/2,j} - (u_1^a)_{i-3/2,j}}{\Delta t} &= -\gamma_1(\phi_{x_1})_{i-3/2,j} \\ \frac{(\tilde{u}_1)_{i-1/2,j} - (u_1^a)_{i-1/2,j}}{\Delta t} &= -\gamma_1(\phi_{x_1})_{i-1/2,j} \\ \frac{(\tilde{u}_1)_{i+1/2,j} - (u_1^a)_{i+1/2,j}}{\Delta t} &= -\gamma_1(\phi_{x_1})_{i+1/2,j} \\ \frac{(\tilde{u}_1)_{i+3/2,j} - (u_1^a)_{i+3/2,j}}{\Delta t} &= -\gamma_1(\phi_{x_1})_{i+3/2,j} \\ \frac{(\tilde{u}_2)_{i,j+1/2} - (u_2^a)_{i,j+1/2}}{\Delta t} &= -\gamma_1(\phi_{x_2})_{i,j+1/2}, \end{aligned} \quad (30)$$

whereas the corrector step for the point $(i, j - \frac{1}{2})$ is given by

$$(\tilde{u}_2)_{i,j-1/2} = 0. \quad (31)$$

Using the divergence operator defined in Eq. (27), Eqs. (30) and (31) can be combined to yield (after making use of the zero divergence condition)

$$\begin{aligned}
 & [-(u_1^a)_{i+3/2,j} + 27(u_1^a)_{i+1/2,j} - 27(u_1^a)_{i-1/2,j} + (u_1^a)_{i-3/2,j}]/(24\Delta x_1) \\
 & + [(u_2^a)_{i,j+1/2}]/(\Delta x_2) \\
 & = \gamma_1 \Delta t [-(\phi_{x_1})_{i+3/2,j} + 27(\phi_{x_1})_{i+1/2,j} \\
 & - 27(\phi_{x_1})_{i-1/2,j} + (\phi_{x_1})_{i-3/2,j}]/(24\Delta x_1) + [(\phi_{x_2})_{i,j+1/2}]/(\Delta x_2)]. \quad (32)
 \end{aligned}$$

Substituting Eqs. (28) and (29) for the gradient operators into Eq. (32), we obtain the difference equation for ϕ at the cell (i, j) . This method of implementing the surface no-slip boundary condition does not require an ad hoc pressure boundary condition. Additional details regarding this boundary condition can be found in Ref. [17].

The predictor step of Eq. (21a) requires the evaluation of the viscous and inviscid terms. Consider for example the term $u_2(u_2)_{x_2}$ of the u_2 momentum equation at the point $(i, j + \frac{1}{2})$. A seven-point stencil of the type used in Eq. (23) cannot be employed at $(i, j + \frac{1}{2})$ because of the proximity of this point to the wall. Hence lower-order accurate finite-differences that require smaller stencils are used in this evaluation as

$$u_2(u_2)_{x_2} = (u_2)_{i,j+1/2} \left(\frac{(u_2)_{i,j+3/2} - (u_2)_{i,j-1/2}}{2\Delta x_2} \right)$$

if $u_2 > 0$;

$$u_2(u_2)_{x_2} = (u_2)_{i,j+1/2} \left(\frac{-(u_2)_{i,j+5/2} + 6(u_2)_{i,j+3/2} - 3(u_2)_{i,j+1/2} - 2(u_2)_{i,j-1/2}}{6\Delta x_2} \right) \quad (33)$$

if $u_2 < 0$. A similar strategy is used for the other derivatives in the x_2 direction that are required in the predictor step of Eq. (21a) and also Eqs. (21b) and (21c).

The periodicity boundary conditions in the streamwise and spanwise directions for the channel flow calculations presented here are straightforward to implement and therefore will not be discussed.

The three-step Runge-Kutta/Crank-Nicholson time-stepping procedure has a stability limit of CFL number $< \sqrt{3}$ for the inviscid part and is A -stable for the viscous part. However, this is true only when central differences are employed in computing the convective terms. The maximum time step for stability is lowered when upwind-biased differences are used to compute the convective terms. A simple Fourier stability analysis of the high-order upwind-biased scheme as applied to the one-dimensional linear convection equation (7) indicates a stability limit of CFL number < 1.43 . However, the scheme remains A -stable for the viscous part.

RESULTS

This section presents results obtained with the high-order accurate upwind scheme discussed earlier. Two test cases have been used to evaluate the accuracy and robustness of this method. These test cases have been chosen based on the availability of results from linear theory, experimental data, and data from previous numerical simulations (spectral method simulations). The test cases are described below.

The first test case consists of calculating the evolution of small-amplitude disturbances in channel flow. In this study the disturbance is taken to be an eigensolution of the Orr–Sommerfeld equation. The advantage of using this problem as a test case is that it has known solutions from linear theory. The flow field is initialized as

$$\begin{aligned} u(x, y, t) &= 1 - y^2 + \varepsilon \tilde{u} \\ v(x, y, t) &= \varepsilon \tilde{v}, \end{aligned} \quad (34)$$

where \tilde{u} , \tilde{v} represent an eigensolution (wavenumber of unity) and $\varepsilon \ll 1$ (0.0001 in this study). The Reynolds number chosen for this calculation Eq. (20) is $\text{Re} = 7500$ (based on mean centerline velocity). The energy associated with the perturbation quantities \tilde{u} and \tilde{v} is defined as

$$E(t) = \int_{-1}^1 \int_0^{2\pi} (\tilde{u}^2 + \tilde{v}^2) dx dy. \quad (35)$$

The energy in the channel $E(t)$ grows exponentially in time as e^{2ct} , and for the Reynolds number and wavenumber chosen the value of c is 0.002235. Additional details regarding this test case can be found in Ref. [21]. In this study the quantity $E(t)/E(0)$ is monitored to determine the adequacy of the accuracy of various schemes.

The second test case is a simulation of fully developed turbulent channel flow. The Reynolds number based on the wall shear velocity (u_τ) is defined by

$$\text{Re}_\tau = \frac{u_\tau \delta}{\nu},$$

where δ is the channel half-width and ν is the kinematic viscosity of the fluid. The Reynolds number used for this calculation (Re_τ) is 180 and is identical to that used in Ref. [8]. The corresponding Reynolds number based on the centerline velocity and channel half-width is 3300. The streamwise and spanwise dimensions of the channel are $4\pi\delta$ and $2\pi\delta$, respectively. The adequacy of these channel dimensions has already been demonstrated in Ref. [8]. The flow field in this case is initialized as

$$\begin{aligned} u(x, y, z, t) &= 1 - y^2 + \varepsilon \tilde{u} \\ v(x, y, z, t) &= \varepsilon \tilde{v} \\ w(x, y, z, t) &= \varepsilon \tilde{w}, \end{aligned} \quad (36)$$

where \tilde{u} , \tilde{v} , and \tilde{w} are obtained from a random number generator (the random numbers are scaled to vary between -1 and 1) and ε is of the order of 0.1 . The governing equations are then integrated in time until the flow field reaches statistical equilibrium.

The grid used in both cases is equispaced in the streamwise and spanwise directions and stretched in the normal direction (wall-to-wall direction). The stretching in the normal direction is based on a geometric progression. Several grid sizes have been used in testing the upwind method and these will be mentioned at the appropriate places in the text. For the sake of brevity, the nonconservative, high-order-accurate scheme described in Eqs. (21) and (22), in which central differences are used to evaluate the viscous terms, upwind biased differences are used for the inviscid terms, and high-order representations are used for the divergence and gradient operators (and also high-order interpolation) will be referred to as scheme A in the remainder of this paper.

Evolution of Small-Amplitude Disturbances

Figure 2 shows the time variation of the perturbation energy in the channel obtained with scheme A and two different grid sizes; the inviscid terms are approximated using upwind-biased differences of third- and fifth-order accuracy. Unlike central difference schemes, all the upwind-biased differences used in this study have leading truncation error terms that are dissipative in nature. Curve 1 shows the energy variation obtained on a (16×65) grid with the inviscid terms

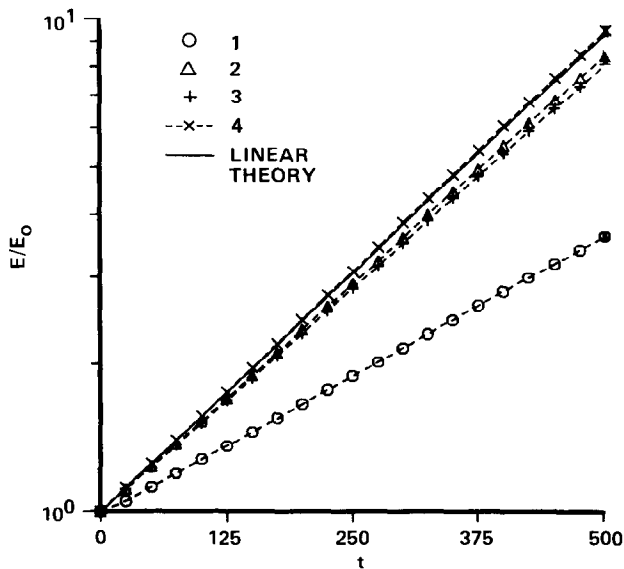


FIG. 2. Energy growth rates for upwind-difference schemes.

evaluated using third-order accurate upwind-biased differences. This energy curve is much lower than the exact one; that is, the calculated energy growth rate is much lower than the exact value. The dissipation has an overwhelming effect on the growth rate of the energy. Curve 2 was obtained with the same scheme but a grid size of (32×65) . The agreement with the exact results is much better although the difference between the two is still noticeable. Curve 3 shows results obtained on a (16×65) grid with the inviscid terms evaluated using fifth-order accurate upwind-biased differences. This curve is almost identical to curve 2, thus indicating that the magnitude of the leading truncation error term in the two cases is approximately the same. Curve 4 shows results obtained with the fifth-order version of scheme A but with a grid size of (32×65) . Curve 4 is almost identical to the exact curve.

The preceding calculations with the upwind-biased schemes indicate that (a) high-order accurate upwind schemes can yield accurate estimates of the evolution of flow instabilities, and (b) they may have the potential of accurately simulating turbulent flow. However, a minimum number of grid points will be required in order to obtain accurate solutions, and this minimum will depend on the order of accuracy of the scheme and the parameters governing the flow. While this information is common knowledge among computational fluid dynamicists, the results shown in Fig. 2 quantify the effects of truncation error on the evolution of small-amplitude disturbances. Results for this test case using central difference schemes can be found in the Appendix.

Coarse-Grid, Upwind-Difference Solutions to Turbulent Channel Flow

The following results were obtained using upwind-biased differences for the inviscid terms (scheme A with fifth-order accurate finite differences) on a $(64 \times 65 \times 64)$ mesh. As discussed earlier, the dissipative nature of the truncation error of such differences controls the aliasing error problem by dissipating the energy content at the higher frequencies. The flow was initialized as in Eq. (36). The computations were initially carried out for approximately 20 nondimensional units of time (tu_τ/δ , where u_τ is the wall shear velocity) upon which statistical equilibrium was reached. The results were then time-averaged over a subsequent period of 23 nondimensional units of time.

The mean velocity distribution nondimensionalized by the wall shear velocity is shown in Fig. 3. The symbols represent the experimental data of Ref. [22] obtained at a Reynolds number of 142 (Re_τ). The experimental data has been rescaled as in Ref. [8]. The dashed line represents the law of the wall and the log law $u^+ = 2.5 \ln(y^+) + 5.5$. The agreement with experiment, the law of the wall, and the log law is good.

The turbulence intensities normalized by the wall shear velocity are shown in wall coordinates in Fig. 4. The symbols in this figure are the experimental data of Ref. [23] for a Reynolds number (Re_τ) of 194. The experimental data have been rescaled as in Ref. [8]. The computed streamwise component u_{rms} is in excess of the experimental data and the computed peak is slightly to the right of the experimental peak. The v_{rms} and w_{rms} profiles are consistently lower than the experimental

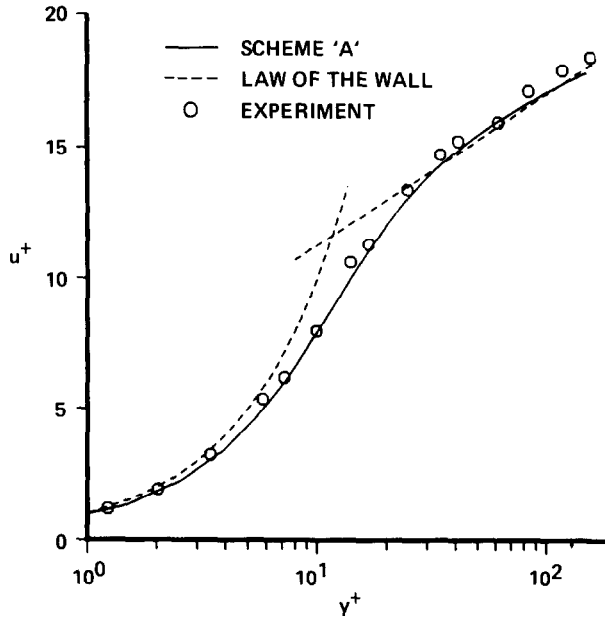


FIG. 3. Mean velocity profiles normalized by wall shear velocity (scheme A; coarse grid).

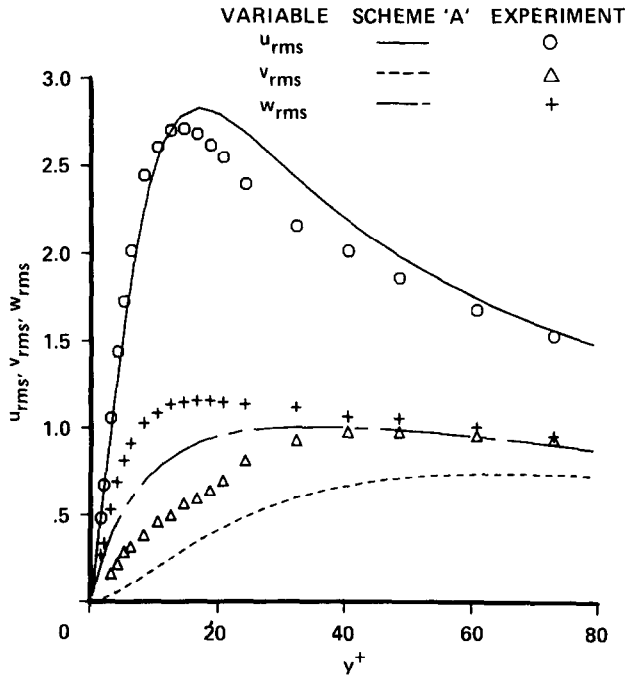


FIG. 4. Root-mean-square velocity fluctuations normalized by the wall shear velocity (wall coordinates, scheme A; coarse grid).

data. The possibility of error in the experimental technique in measuring v_{rms} (resulting in larger measured values of this quantity), is discussed in Ref. [8] and will not be repeated here. The more recent experimental data of Ref. [24] shows v_{rms} data that are lower than those of Ref. [23]. These data are presented later in the paper in conjunction with the fine-grid computational data.

The turbulence intensities normalized by the local mean streamwise velocity are shown in Fig. 5. The symbols represent the experimental data of Refs. [23, 25]. As pointed out in Ref. [8], the limiting values of these quantities at the wall approach the vorticity fluctuation values normalized by the mean velocity gradient at the wall (a comparison will be made later in the paper). The comparison between the experimental and computational data is approximately of the same quality as that obtained in the spectral simulation of Ref. [8]. The limiting value of u_{rms} at the wall is about 0.36, which is the same as that reported in Ref. [8]. The normal and spanwise components of intensity are slightly lower than those reported in Ref. [8].

Vorticity fluctuations normalized by the mean shear at the wall ($\omega_i v / (u_\tau)^2$) in wall coordinates are shown in Fig. 6 along with the spectral results of Ref. [8] (obtained using a $192 \times 129 \times 160$ grid). Vorticity, for data obtained using scheme A, was calculated using a sixth-order accurate central difference on a seven-point stencil. Small scale motions contribute significantly to vorticity and, therefore, computing vorticity fluctuations accurately constitutes an exacting test of the computational method. The finite-difference results agree qualitatively with the

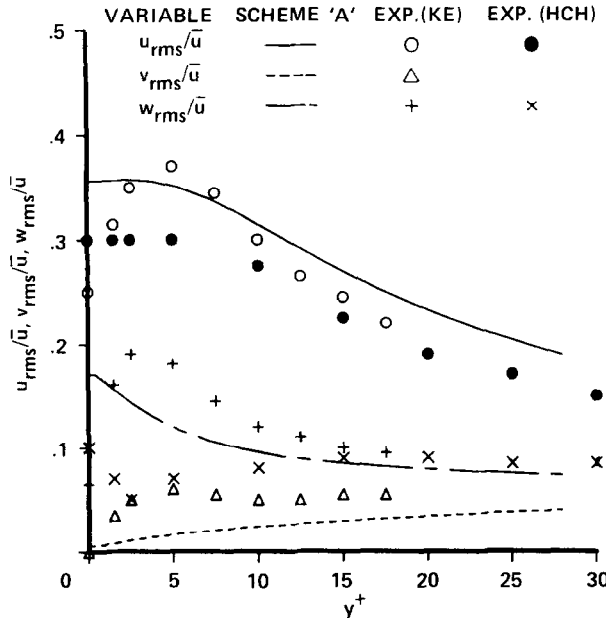


FIG. 5. Root-mean-square velocity fluctuations normalized by the local mean velocity (wall coordinates, scheme A; coarse grid).

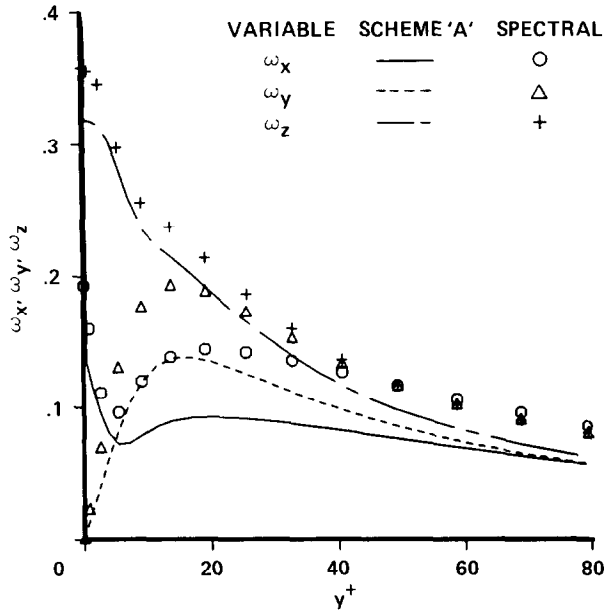


FIG. 6. Root-mean-square vorticity fluctuations normalized by the mean shear (wall coordinates, scheme A; coarse grid).

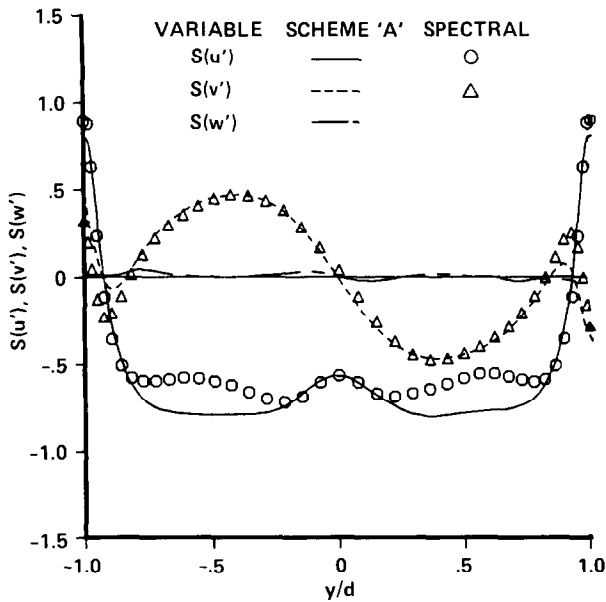


FIG. 7. Skewness factors (global coordinates, scheme A; coarse grid).

spectral results of Ref. [8]. All three components are seen to be lower than their spectral counterparts. This observation is consistent with the fact that scheme A is dissipative in nature.

Figure 7 shows skewness factors for the velocity fluctuations in global coordinates obtained in the present calculation and those reported in Ref. [8]. The skewness factors are defined as

$$S(u') = \overline{(u')^3} / (\overline{(u')^2})^{3/2}$$

$$S(v') = \overline{(v')^3} / (\overline{(v')^2})^{3/2}$$

$$S(w') = \overline{(w')^3} / (\overline{(w')^2})^{3/2}.$$

The two sets of results are in fair agreement with each other; for example, the u -profile crosses the zero line at $y^+ = 12$, the spectral result being $y^+ = 13$. However, there are differences between the spectral and scheme A results because of the coarseness of the grid used in the finite-difference simulation.

Results of the type shown in Figs. 3–7 that were obtained using a second-order accurate central difference scheme are presented in the Appendix. A comparison of the results obtained using scheme A and the central difference method shows that, in general, scheme A yields better results. More importantly, the scheme A results

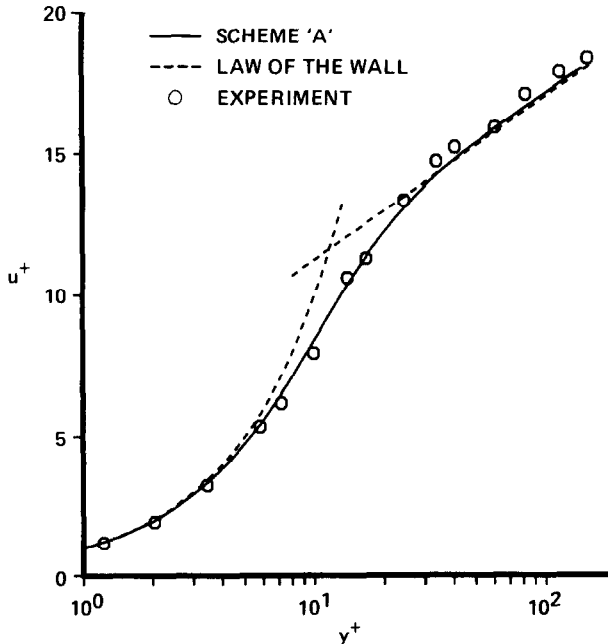


FIG. 8. Mean velocity profiles normalized by wall shear velocity (scheme A; fine grid).

were obtained without an aliasing-error control mechanism such as a kinetic energy conservation principle or a method requiring Fourier decomposition techniques with the attendant limitations regarding grid uniformity.

Fine-Grid, Upwind-Difference Solutions to Turbulent Channel Flow

The coarse-grid computations with scheme A were repeated on a fine grid with grid dimensions of $(192 \times 101 \times 192)$. This computation was performed to make direct comparisons with the data of Ref. [8] (which were obtained on a grid of the size $(192 \times 129 \times 160)$). The results presented below follow along the lines of the earlier presentation, and, while this exercise may appear repetitious, it does provide a detailed demonstration that accurate direct simulations can be performed with high-order accurate, upwind-biased, finite-difference schemes.

Figure 8 shows the mean velocity distribution in the channel. The agreement with the experimental data and the law of the wall is good. The turbulence intensities normalized by the wall shear velocity are shown in wall coordinates in Fig. 9. The computed data are compared with experimental data as in Fig. 4. The computed streamwise component u_{rms} is in good agreement with the experimental data. The

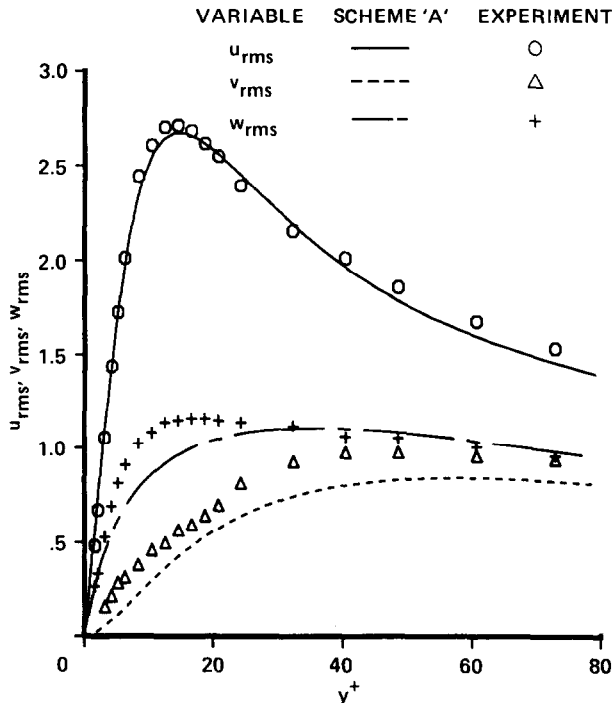


FIG. 9. Root-mean-square velocity fluctuations normalized by the wall shear velocity (wall coordinates, scheme A; fine grid). Comparison with experimental data.

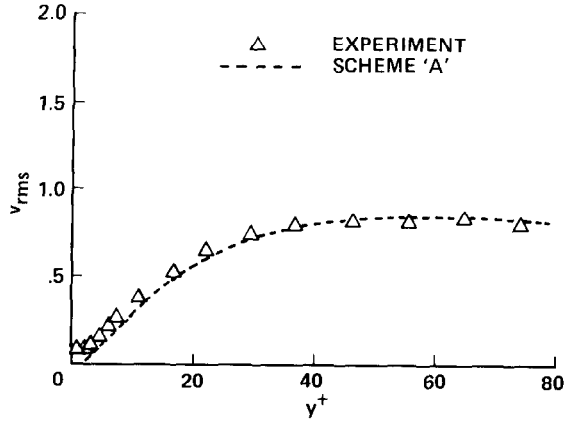


FIG. 10. Root-mean-square "v" velocity fluctuations normalized by the wall shear velocity (wall coordinates, scheme A; fine grid). Comparison with experimental data.

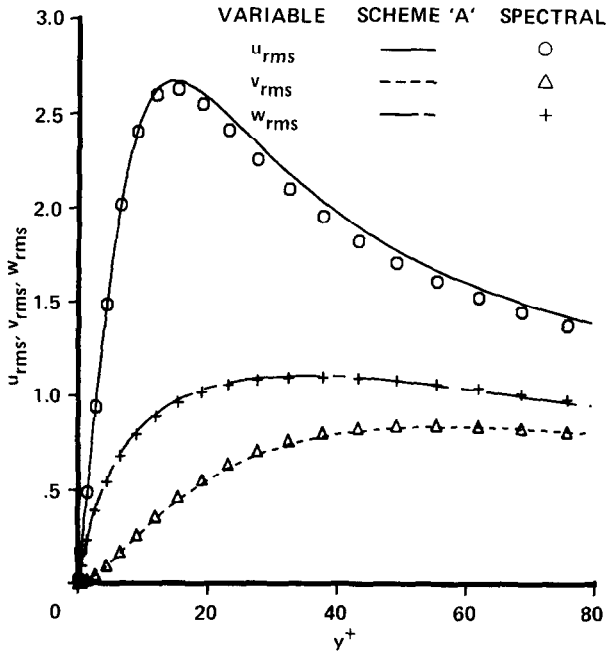


FIG. 11. Root-mean-square velocity fluctuations normalized by the wall shear velocity (wall coordinates, scheme A; fine grid). Comparison with spectral data.

normal and spanwise components, v_{rms} and w_{rms} , are in better agreement with the experiment than in Fig. 4. Figure 10 shows the computed v_{rms} profile along with the recent experimental data of Ref. [24] obtained using an LDV technique at a Reynolds number (Re_τ) of 178.6. The agreement between the two sets of data is good. The agreement between the computed u_{rms} profile and the corresponding experimental data of Ref. [24] is of the same quality as in Fig. 9.

Figure 11 shows a comparison of the turbulence intensities obtained with scheme A and the spectral data of Ref. [8]. All three components computed by scheme A are seen to be in good agreement with the spectral data. Figure 12 shows the computed and experimental turbulence intensities normalized by the local mean streamwise velocity. The agreement with experiment is better than in Fig. 5. These same computed intensities are compared with the spectral data of Ref. [8] in Fig. 13. The present data are in good agreement with the spectral data.

The near wall behavior of the turbulence intensities and Reynolds shear stress are shown in Fig. 14. This figure also shows the spectral data of Ref. [8]. The quantities u_{rms} and w_{rms} are normalized with y^+ , v_{rms} with $(y^+)^2/10$, and the Reynolds shear stress with $(y^+)^3/400$. This figure shows the limiting linear behavior of the tangential stresses in the near-wall region and the quadratic behavior of the normal stress in the region $0.5 < y^+ < 7.5$. The u_{rms} , v_{rms} , and w_{rms} profiles are in good agreement

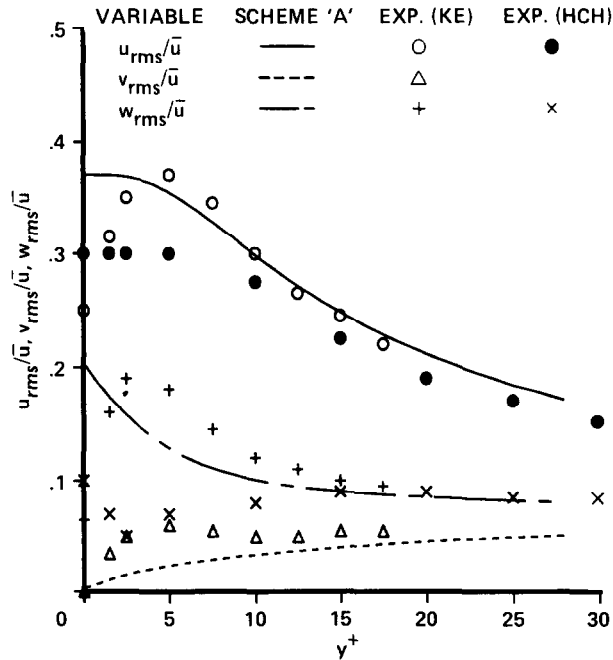


FIG. 12. Root-mean-square velocity fluctuations normalized by the local mean velocity (wall coordinates, scheme A; fine grid). Comparison with experimental data.

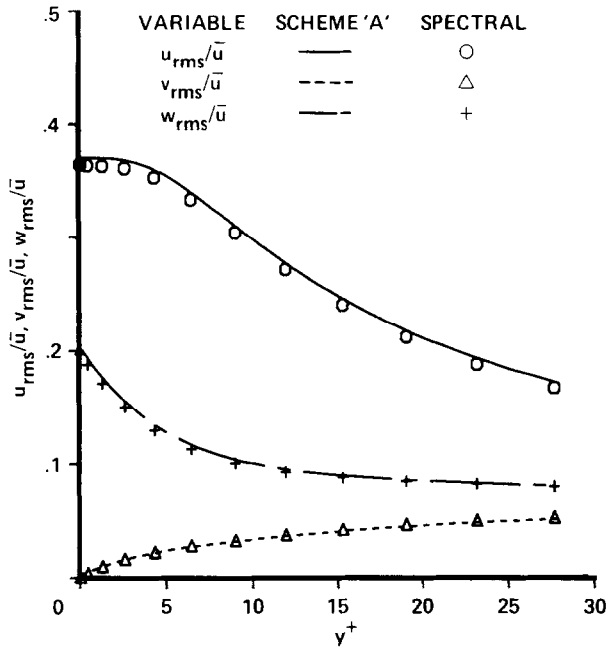


FIG. 13. Root-mean-square velocity fluctuations normalized by the local mean velocity (wall coordinates, scheme A; fine grid). Comparison with spectral data.

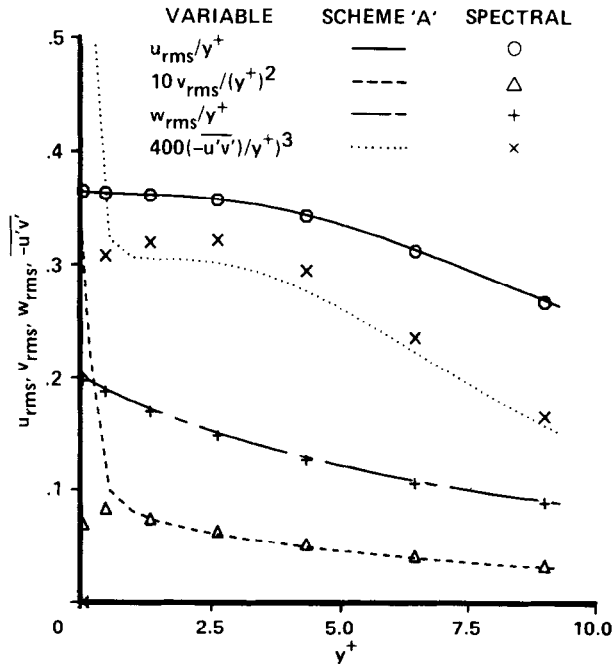


FIG. 14. Near wall behavior of Reynolds stresses (wall coordinates, scheme A; fine grid).

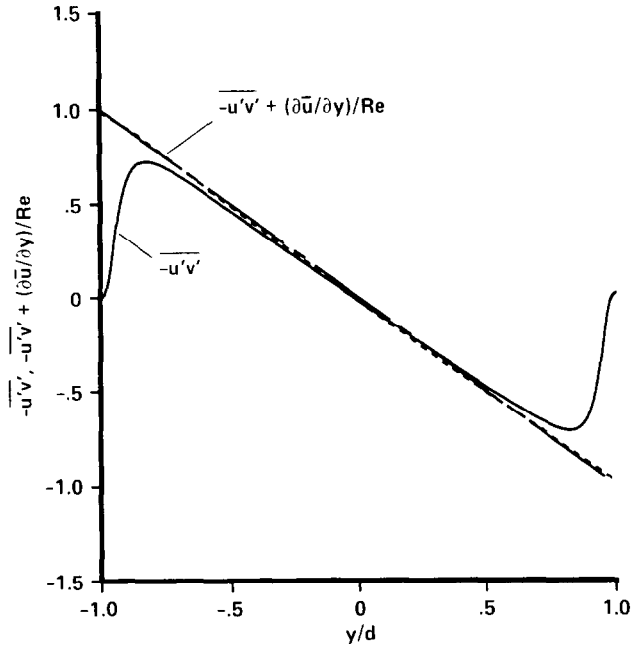


FIG. 15. Reynolds shear stress and total shear stress profiles normalized by the square of the wall shear velocity (global coordinates, scheme A, fine grid).

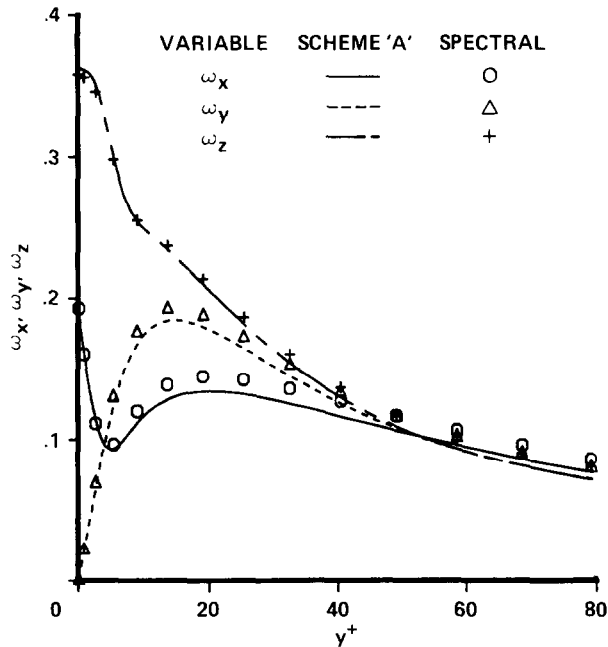


FIG. 16. Root-mean-square vorticity fluctuations normalized by the mean shear (wall coordinates, scheme A; fine grid).

with the data of Ref. [8]. The Reynolds shear stress values obtained with scheme A are slightly lower than those of Ref. [8].

Figure 14 shows a change in behavior in the normal stress and Reynolds shear stress very close to the wall. One possible reason for this anomalous behavior is that the finite-difference scheme is second-order accurate near the wall. In addition, $y^+ = dy^+$ for the grid point just above the wall surface and therefore a division by $(y^+)^2$ is identical to a division by $(dy^+)^2$. Hence a division of the normal stress by $(y^+)^2$ would result in a quantity that is zeroth-order accurate near the boundary. A similar explanation holds true for the anomaly in the near wall behavior of the Reynolds shear stress. However, it should be noted that two grid points away from the wall the computed normal stress and Reynolds shear stress values agree well with the spectral data.

Figure 15 shows the computed Reynolds shear stress and total shear stress profiles in global coordinates. The total stress profile should assume a straight line distribution when the flow reaches statistical equilibrium (shown as a chain-dashed line in Fig. 15). The computed total stress curve (dashed line) is seen to coincide with this line, indicating that the present computation has reached statistical equilibrium.

Figure 16 shows vorticity fluctuations normalized by the mean shear at the wall as in Fig. 6. Clearly the agreement between the finite-difference and spectral data is good and, furthermore, better than the agreement seen in Fig. 6. The wall value of

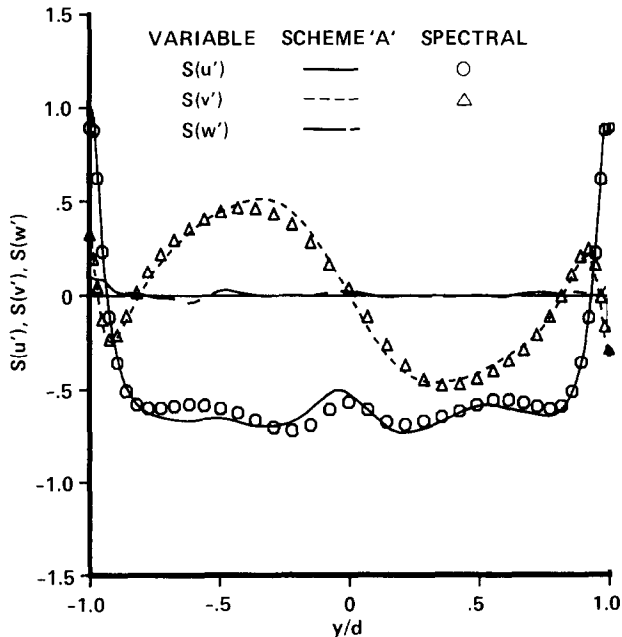
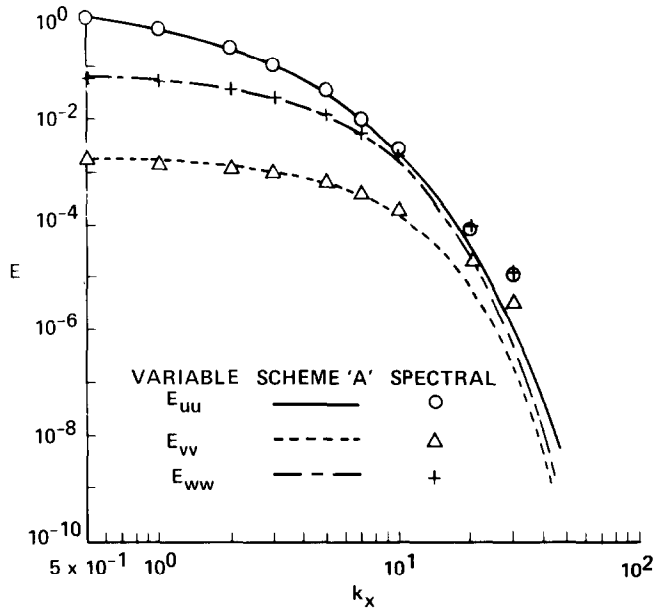
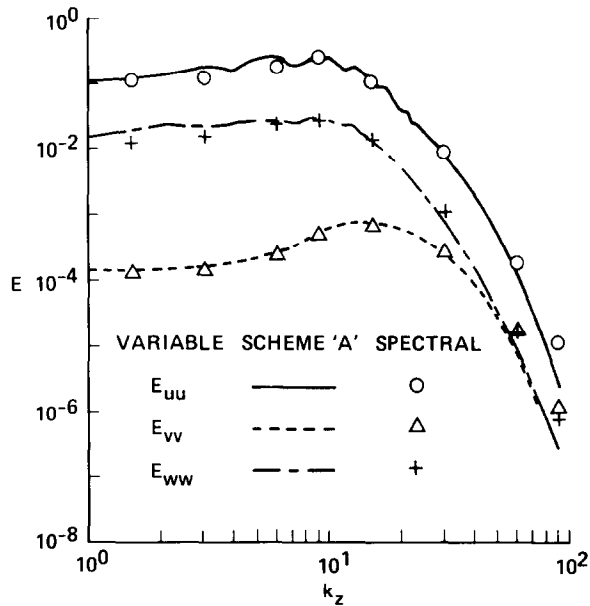


FIG. 17. Skewness factors (global coordinates, scheme A; fine grid).

FIG. 18. One-dimensional streamwise energy spectra at $y^+ = 5.39$ (scheme A; fine grid).FIG. 19. One-dimensional spanwise energy spectra at $y^+ = 5.39$ (scheme A; fine grid).

the streamwise component is 0.19 and the peak in the normal component is 0.19 (the corresponding values from Ref. [8] are 0.19 and 0.20, respectively).

Skewness factors of the velocity fluctuations are presented in Fig. 17 as in Fig. 7. The scheme A results compare well with the spectral data and also show an improvement over the coarse grid results of Fig. 7.

Figures 18 and 19 show energy spectra at the location $y^+ = 5.39$ obtained in the current calculation and those of Ref. [8]. The quantities k_x and k_z in these figures are the wavenumbers in the streamwise and spanwise directions, respectively. The energy densities are defined as

$$E_{uu}(k_x) = \sum_{k_z} \hat{u}(k_x, k_z) \hat{u}^*(k_x, k_z)$$

$$E_{uu}(k_z) = \sum_{k_x} \hat{u}(k_x, k_z) \hat{u}^*(k_x, k_z),$$

where the \hat{u} values are obtained from the Fourier decomposition of the perturbation velocity u' ,

$$\hat{u}(k_x, k_z) = \sum_{x, z} u'(x, z) e^{-ik_x x} e^{-ik_z z}.$$

Similar expressions are used to obtain the energy spectra of the other velocity components. The energy densities obtained with scheme A at the higher wavenumbers

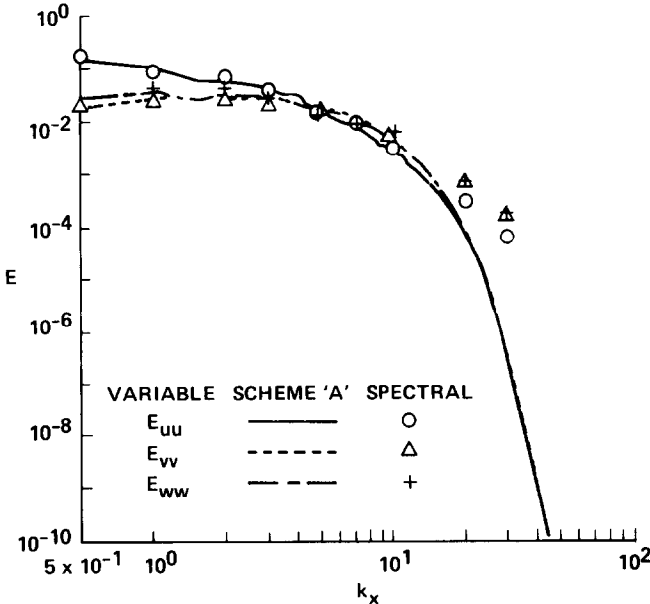


FIG. 20. One-dimensional streamwise energy spectra at $y^+ = 149.23$ (scheme A; fine grid).

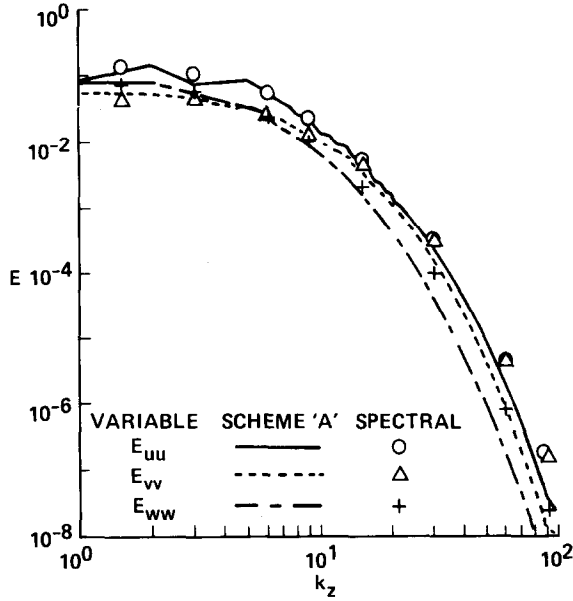


FIG. 21. One-dimensional spanwise energy spectra at $y^+ = 149.23$ (scheme A; fine grid).

are lower than those predicted by the spectral calculation of Ref. [8]. This is consistent with the high-wavenumber dissipative nature of scheme A. Neither of these figures indicate an accumulation of energy at the high wavenumbers; both streamwise and spanwise distributions show a decrease in energy density with increasing wavenumber. Figures 20 and 21 show energy spectra at $y^+ = 149.23$. The energy spectra in these two figures exhibit the same characteristic (dissipation at higher wavenumbers and absence of energy accumulation) as in Figs. 18 and 19.

In general the fine grid results are in good agreement with both the experimental data and the computed results of Ref. [8]. As expected the fine grid results are closer to the experimental data and the results of Ref. [8] than the coarse grid results. Whereas the spectral method possesses the highest accuracy for a given number of grid points, the high-order accurate upwind-biased, finite-difference method seems to yield solutions of comparable accuracy.

SUMMARY

The prevalent method for direct simulations of turbulent flow is the spectral method. Whereas the spectral method is extremely accurate, it places restrictions on the type of geometry and grids that can be efficiently handled. The current study presents a high-order accurate finite-difference approach for calculating incompressible turbulent flow. Unlike the spectral method, the finite-difference method

can be used efficiently with curvilinear grids (although the method is developed for stretched Cartesian grids in the current study).

The finite-difference method is evaluated using two test cases; the evolution of small-amplitude disturbances and fully developed turbulent channel flow. Results obtained for the first test case indicate the need for high-order accuracy. These results also serve to quantify grid requirements in order to obtain accurate results with finite-difference schemes of various orders of accuracy. Results obtained for the turbulent channel flow calculation demonstrate the need for aliasing error-control mechanisms when the inviscid terms in the momentum equations are evaluated using central differences. The calculations with central differences were discontinued because the aliasing error-control procedures currently available require either a kinetic energy conservation principle (which at present conflicts with the need for high-order accuracy on general grids) or a Fourier decomposition of the data (which has all the limitations of the spectral method).

The high-order accurate upwind methods are naturally dissipative in nature and were found to control aliasing error at the expense of some accuracy. However, for the grid size used ($192 \times 101 \times 192$), the upwind method yielded mean flow properties as well as first- and second-order statistics that agreed well with both experimental data and earlier spectral simulations. While the shortcoming of the upwind method (numerical dissipation) can be overcome by using additional grid points, the limitations of the spectral method are more fundamental in nature. The use of the central difference schemes depends on whether general-purpose aliasing error-control procedures can be found. The upwind difference code requires roughly the same amount of computing time per grid point for each substep in the Runge-Kutta scheme as the spectral simulations of Ref. [8] (without a major effort at code optimization). It is believed that the finite difference codes can be made more cost effective on a per-grid-point basis than spectral codes. The computing cost issue is deferred for further study. At present it appears that the high-order accurate upwind-biased method is a good candidate for direct simulations of turbulent flows associated with complex geometries. Although only one particular type of upwind-biased finite-difference scheme has been extensively tested in this study and found to yield accurate simulations of turbulent flow, other similar schemes with different biasing and stencils may be equally effective.

APPENDIX

The second-order accurate central-difference method has found use in direct and large-eddy simulations of turbulent flow. In order that comparisons can be made between the predictive capabilities of the high-order accurate upwind method and central difference schemes this section includes results obtained with central-difference schemes, for fully developed turbulent channel flow and the evolution of small amplitude disturbances.

As discussed earlier, central difference schemes must be kinetic-energy conserving

in their formulation or have some other aliasing error control mechanism in order to yield stable solutions when computing turbulent flow. The method of Ref. [17] with the convective terms as evaluated in Ref. [11] is kinetic-energy conserving and is second-order accurate. A variant of this method (three-step Runge–Kutta/Crank–Nicholson time-stepping instead of the Adams–Bashforth/Crank–Nicholson time-stepping of Ref. [17]) is one of the schemes used in this study. This scheme will be referred to as scheme B throughout this Appendix. It should be noted that scheme B uses the conservative form of the governing equations for its formulation.

The nonconservative, high-order accurate scheme described in Eqs. (21) and (22), in which central differences are used to evaluate the viscous terms, upwind biased differences are used for the inviscid terms, and high-order representations are used for the divergence and gradient operators (and also high-order interpolation) was referred to as scheme A earlier in the text. Scheme C in this study is similar to scheme A except that the high-order accurate differences that are used to evaluate the inviscid terms are central differences. Scheme C, although stable on equispaced grids, can be unstable on stretched grids because of the appearance of the diagonal elements in the difference formulas as in Eq. (12) (private communication, Dr. J. L. Steger, NASA Ames Research Center). However, depending on the Reynolds number, the viscous terms of the Navier–Stokes equations may provide sufficient damping to stabilize the scheme. Results obtained for the evolution of small-amplitude disturbances with schemes B and C are presented below followed by results for fully developed turbulent channel flow with scheme B.

Evolution of Small-Amplitude Disturbances

Figure 22 shows the time variation of the energy E (Eq. (35)) in the channel for the growing eigensolution problem obtained using central difference schemes. The grid size used for all the calculations shown in Fig. 22 is (32×65) . The finite-difference solutions are compared with the solution from linear theory in Fig. 22. The energy curve obtained with scheme B (curve 1) is much lower than the exact curve; that is, the calculated energy growth rate is much lower than the exact value. Malik *et al.* [21] present energy growth rate results for the same problem but obtained them using a spectral method in the streamwise direction and second-order accurate central differences in the normal direction. The ratio of energies was found to decrease instead of increasing as in curve 1 for the same number of grid points in the normal direction (an even worse situation in comparison with the exact curve). The more inaccurate results of Ref. [21] may be in part due to the distribution of grid points in the normal direction. Reference [21] uses a distribution based on the cosine function while the current study uses a geometric progression. The cosine distribution is inappropriate for finite-difference simulations because the rate of change of grid spacing can be relatively high at the walls. In addition to the grid sensitivity, Scheme B was also found to be sensitive to the order of accuracy of the interpolation scheme that is used in conjunction with the staggered grid, the differencing formulae used at the walls, and other parameters.

Curve 2 of Fig. 22 represents the solution obtained with scheme C with the

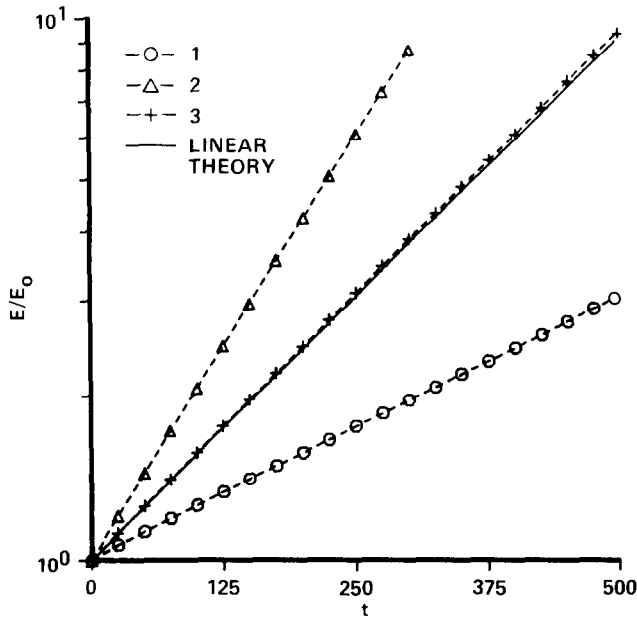


FIG. 22. Energy growth rates for central-difference schemes.

inviscid terms evaluated using second-order-accurate central differences. The growth rate in this case is much higher than the actual value. The fact that curve 2 lies above the exact curve and curve 1 lies below the exact curve indicates that variants of the methods used to generate these two curves may (because of a fortuitous balance of the dispersive and dissipative errors) yield solutions that seem superior. However, such an improvement would be highly case-dependent.

Curve 3 shows the growth rate obtained with scheme C and the inviscid terms evaluated with fourth-order accurate finite differences. The higher order of accuracy results in a solution that is very close to the exact curve over a time period corresponding to an energy increase of an order of magnitude. Figure 22 clearly indicates the need for high-order accuracy in order to accurately predict the growth of instabilities. It should be noted that scheme C cannot be used for direct simulations of turbulence without resorting to aliasing error-controlling mechanisms. Scheme C is stable for this particular test case because it is being used to resolve a single sine wave in the streamwise direction (the energy content of the higher frequencies is zero and hence the aliasing error problem does not arise in this case).

Coarse-Grid, Central-Difference Solutions to Turbulent Channel Flow

The following results for fully developed turbulent channel flow were obtained with scheme B on a $(64 \times 65 \times 64)$ mesh. The flow field was initialized using the computed data obtained from the coarse-grid upwind method solution reported

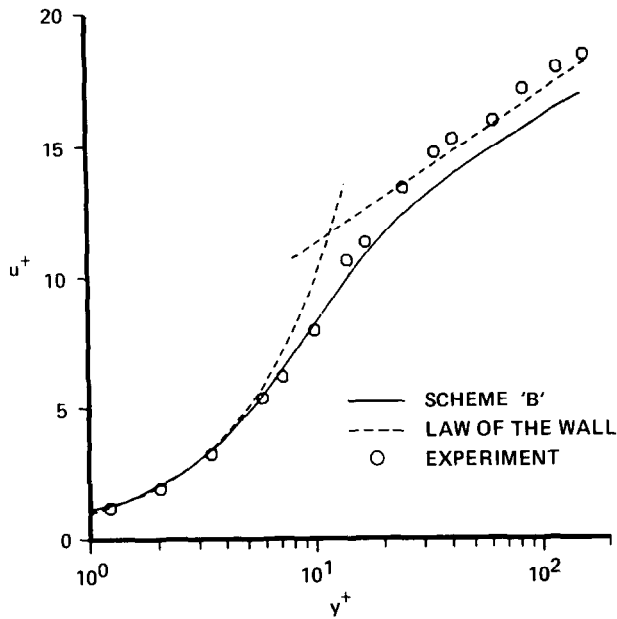


FIG. 23. Mean velocity profiles normalized by wall shear velocity (scheme B).

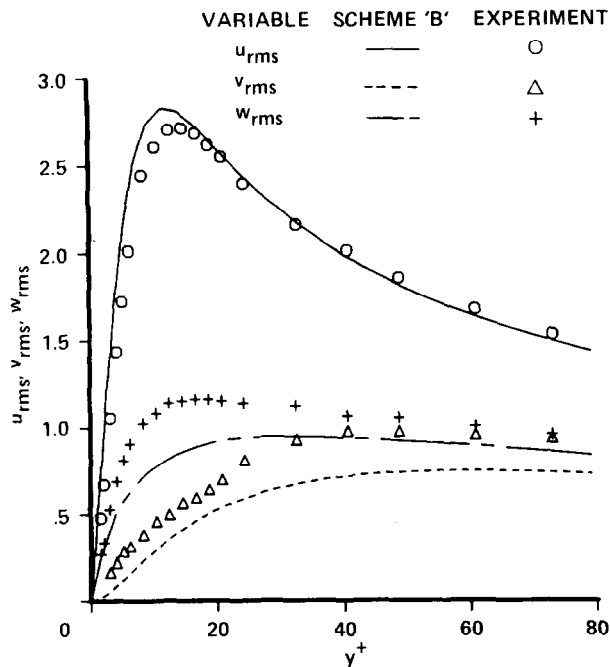


FIG. 24. Root-mean-square velocity fluctuations normalized by the wall shear velocity (wall coordinates, scheme B).

earlier. The calculations were initially carried out for approximately 10 nondimensional units of time after which statistical equilibrium was reached. The results were then time-averaged over a subsequent period of 10 nondimensional units of time.

The mean velocity distribution nondimensionalized by the wall shear velocity is shown in Fig. 23. The agreement between the present calculation and the experimental results is unsatisfactory. The inaccuracies of the method seem to distort not only the turbulence statistics (as will be seen in later figures) but even mean-flow quantities such as the mass flow through the channel. The results shown in Fig. 23 can be directly compared with those of Fig. 3. The high-order accurate upwind method is seen to yield superior results.

Figure 24 shows turbulence intensities plotted against wall coordinates as in Fig. 4. The computed u_{rms} profile is in fairly good agreement with the experimental data and slightly better than that obtained with the high-order accurate upwind method. However, the v_{rms} and w_{rms} profiles are consistently lower than the experimental data. The w_{rms} profile is better predicted by scheme A, whereas the v_{rms} profile is better predicted by scheme B. However, the differences between the results obtained from schemes A and B are slight and hence the turbulence intensities do not seem to indicate the superiority of either of these methods.

The turbulence intensities normalized by the local mean streamwise velocity are

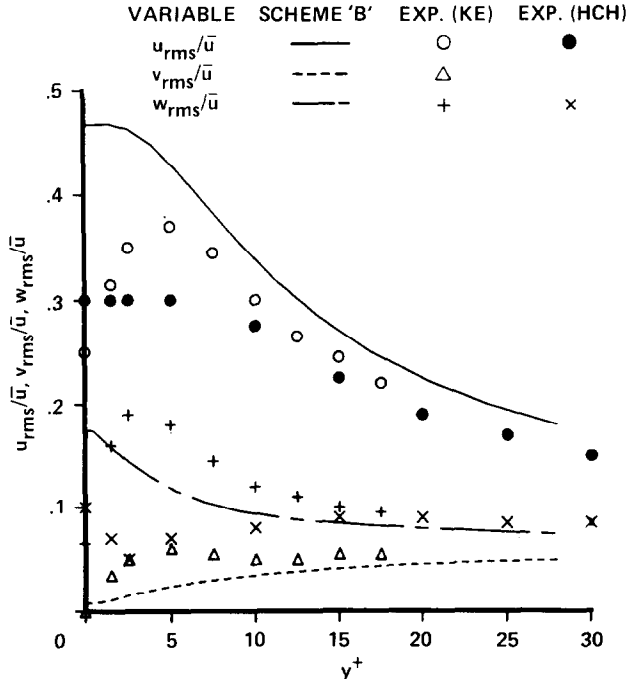


FIG. 25. Root-mean-square velocity fluctuations normalized by the local mean velocity (wall coordinates, scheme B).

shown in Fig. 25. While the comparison between the experimental and computational data is approximately of the same quality as that obtained in the spectral simulation of Ref. [8] for v_{rms} and w_{rms} , the computed limiting value of u_{rms} is much higher than the experimental data and that reported in Ref. [8] (the present value is 0.46 and that of Ref. [8] is 0.36). A comparison of the results presented in Figs. 5 and 25 shows that overall scheme A yields superior results for the intensities in the near wall region.

Vorticity fluctuations normalized by the mean shear at the wall in wall coordinates are shown in Fig. 26. These vorticity values were obtained using three-point central differences (consisting with the differencing stencil used for the convective and viscous terms). These results agree qualitatively with the spectral results of Ref. [8]. However, the computation with scheme B yields a spanwise component that is too large in the region $y^+ < 15$; the wall value being about 0.46 instead of the reported value of 0.36 of Ref. [8]. In contrast, the computed streamwise and normal components of vorticity fluctuations are much smaller than those obtained in Ref. [8]. The wall value of the streamwise component in Fig. 26 is 0.12 as opposed to a value of 0.19 in Ref. [8], and the maximum in the normal component is about 0.12 instead of the 0.2 reported in Ref. [8]. A comparison of these results with those obtained with scheme A (Fig. 6) shows that the streamwise and normal components obtained with the two schemes are approximately the same, whereas the spanwise component is computed more accurately with scheme A.

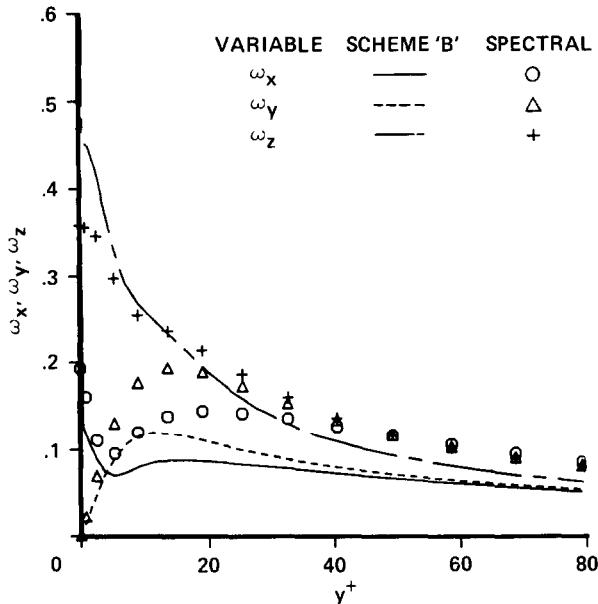


FIG. 26. Root-mean-square vorticity fluctuations normalized by the mean shear (wall coordinates, scheme B).

Figure 27 shows the computed skewness factors of the velocity fluctuations in global coordinates along with the results of Ref. [8]. There are several differences between the present computation and those of Ref. [8], a few of which are mentioned below. The u -profile crosses the zero line first at $y^+ = 35$ in Fig. 27, instead of crossing it at $y^+ = 13$ as in Ref. [8]. The wall value of the u profile is about 2.40 in the current study, whereas the spectral simulation of Ref. [8] yields a value of approximately 0.90. In general the curves of Fig. 27 compare with the data of Ref. [8] only in a qualitative manner. A comparison of the results of Figs. 7 and 27 shows that the results obtained with scheme A are significantly better than those obtained with scheme B.

Clearly the results obtained from scheme B on a $(64 \times 65 \times 64)$ grid are unsatisfactory. Increasing the grid resolution would certainly improve the results. However, this path was not pursued, because it is not clear whether this method can be made high-order accurate on generalized grids without the loss of the kinetic energy conservation property. Instead, scheme C (which can be made high-order accurate on general grids) in which the inviscid terms are approximated with sixth-order accurate central differences was investigated and found to be unstable for the turbulent channel flow calculation. This unstable behavior is caused at least in part by aliasing errors. A scheme to remove aliasing error at each time step, based on Fourier decomposition techniques and the $\frac{3}{2}$ rule, stabilized the method. However,

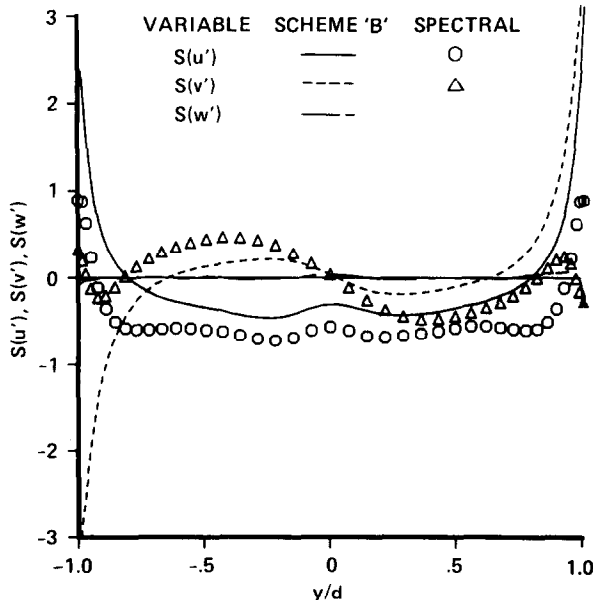


FIG. 27. Skewness factors (global coordinates, scheme B).

since series representation methods of removing aliasing error, such as the Fourier decomposition method, are impractical for curvilinear grids, this approach was discontinued.

ACKNOWLEDGMENTS

The authors would like to thank Dr. R. Moser, Dr. J. Kim, Dr. J. L. Steger, and Dr. R. M. Beam of NASA Ames Research Center for the many helpful discussions they have had with them during the course of this investigation.

REFERENCES

1. J. FLORES, N. M. CHADERJIAN, AND R. L. SORENSON, AIAA Paper 87-1199, 1987.
2. M. M. RAI, *AIAA J. Propulsion and Power* **3** (1989).
3. R.-J. YANG, J. L. C. CHANG, AND D. KWAK, AIAA Paper 87-0368, 1987.
4. K.-Y. CHIEN, *AIAA J.* **20** (1982).
5. B. S. BALDWIN AND H. LOMAX, AIAA Paper 78-257, 1978.
6. D. DEGANI AND L. B. SCHIFF, AIAA Paper 83-0034, 1983.
7. J. H. FERZIGER, *AIAA J.* **15** (1977).
8. J. KIM, P. MOIN, AND R. MOSER, *J. Fluid Mech.* **177** (1987).
9. K. Z. KORCZAK AND A. T. PATERA, *J. Comput. Phys.* **62** (1986).
10. J. W. DEARDORFF, *J. Fluid Mech.* **41** (1970).
11. F. H. HARLOW AND J. E. WELCH, *Phys. Fluids* **8** (1965).
12. J. LAUFER, NACA Report 1053, 1950.
13. U. SCHUMANN, *J. Comput. Phys.* **18** (1975).
14. G. COMTE-BELLOT, No. 419, Publ. Sci. et Techn. du Ministere de l'Air, 1965.
15. J. R. HERRING, S. A. ORSZAG, R. H. KRAICHNAN, AND D. G. FOX, *J. Fluid Mech.* **66** (1974).
16. M. M. RAI, AIAA Paper 87-0543, 1987.
17. J. KIM AND P. MOIN, *J. Comput. Phys.* **59** (1985).
18. A. J. CHORIN, *Math. Comput.* **23** (1969).
19. C. CANUTO, M. Y. HUSSAINI, A. QUARTERONI, AND T. A. ZANG, *Spectral Methods in Fluid Dynamics* (Springer-Verlag, New York, 1988).
20. A. A. WRAY, Minimal storage time-advancement schemes for spectral methods, *J. Comput. Phys.*, submitted for publication.
21. M. R. MALIK, T. A. ZANG, AND M. Y. HUSSAINI, *J. Comput. Phys.* **61** (1985).
22. H. ECKELMANN, *J. Fluid Mech.* **65** (1974).
23. H. KREPLIN AND H. ECKELMANN, *Phys. Fluids* **22** (1979).
24. M. A. NIEDERSCHULTE, Ph.D. thesis, Department of Chemical Engineering, University of Illinois at Urbana-Champaign, 1989.
25. T. J. HANRATTY, L. G. CHORN, AND D. T. HATZIVRAMIDIS, *Phys. Fluids* **20** (1977).